



# 3D-printed graphene-anatase TiO<sub>2</sub> photoanode with well-interconnected hierarchical channels for integrated self-floating photofuel cell powered by seawater pollutants

Zhengpeng Yang<sup>a,1</sup>, Xinyin Yang<sup>a,b,1</sup>, Meng Zhu<sup>b,1</sup>, Yutao Niu<sup>b,c</sup>, Chunjing Zhang<sup>a</sup>, Ping Li<sup>a</sup>, Yongyi Zhang<sup>b,c,d,\*</sup>, Zhichao Xu<sup>a</sup>, Qingwen Li<sup>b,c,\*</sup>

<sup>a</sup> Henan Key Laboratory of Materials on Deep-Earth Engineering, School of Materials Science and Engineering, Henan Polytechnic University, Jiaozuo 454003, China

<sup>b</sup> Key Laboratory of Multifunctional Nanomaterials and Smart Systems, Advanced Materials Division, Suzhou Institute of Nano-Tech and Nano-Bionics, Chinese Academy of Sciences, Suzhou 215123, China

<sup>c</sup> School of Nano-Tech and Nano-Bionics, University of Science and Technology of China, Hefei 230026, China

<sup>d</sup> Division of Nanomaterials and Jiangxi Key Lab of Carbonene Materials, Jiangxi Institute of Nanotechnology, Nanchang 330200, China

## ARTICLE INFO

### Keywords:

3D printing  
Integrated photofuel cell  
Well-interconnected oriented channels  
Self-floating  
Seawater pollutants

## ABSTRACT

Photoelectrode architecture with well-interconnected oriented micro- and nanochannels is essential and critical for photofuel cell (PFC) to high-performance energy conversion of pollutants. However, challenges remain pertaining to manufacturing consistency and scalability, high efficiency in pollutant trapping and remarkable light absorption. Herein, a novel photoelectrode featuring porous microlattice structure was constructed via a scalable and controllable extrusion-based 3D printing strategy, with well-interconnected oriented channels as well as enriched hierarchical and open pores built by jointing tortuous photoactive graphene sheets. The unique architectural features facilitated high light absorption, and meanwhile guaranteed unimpeded channels acting as “superhighways” for rapid seawater pollutant diffusion and trapping. An integrated PFC assembled with 3D-printed photoelectrode demonstrated impressive photoelectric conversion capability for seawater pollutants under persistent self-floating and sunlight, with exceptional cycling stability and maximum power density of 0.09 mW cm<sup>-2</sup>. This work has shed light on new strategies for fabricating rational photoelectrode architectures toward high-performance PFC devices.

## 1. Introduction

Photofuel cells (PFCs) are an important type of energy conversion devices which use light and biomass to generate electrical energy through simultaneous conversion of light and chemical energy. These fuel cells have recently stimulated wide interest in the research communities owing to their capability to harvest solar energy especially when they use environmental pollutants as the source of chemical energy [1–6]. To pursue higher energy conversion for meeting ever-growing practical demands, various photocatalysts have been widely explored for photoactive electrodes, including metal oxides, sulfides and oxynitrides [7–12], and noble metal based plasmonic photoelectrodes [13,14]. Nevertheless, the ineffective transportation and trapping of pollutants as well as poor harvesting and absorption of

incident light are yet two long-standing issues, especially at a large electrode thickness, dramatically hampering the efficient energy conversion and large-scale practical applications [15]. The key to address these limitations and achieve high-performance energy conversion systems lies in fabricating effective and rational photoelectrode architectures that exhibit remarkable light absorption and abundant sites for binding of environmental pollutants.

Recent years have witnessed tremendous endeavors in the exploration of the photoelectrode structures for developing superior PFC devices [16–19]. A general strategy for constructing the photoelectrode is to directly grow nano-photocatalysts onto planar conductive substrates (e.g., metal foil, indium-tin-oxide and fluorine-doped tin oxide) via a variety of methods, such as hydrothermal, solvothermal, low-temperature sintering and electron bombardment processes

\* Correspondence to: Suzhou Institute of Nano-Tech and Nano-Bionics, Chinese Academy of Sciences, Suzhou 215123, China.

E-mail addresses: [yyzhang2011@sinano.ac.cn](mailto:yyzhang2011@sinano.ac.cn) (Y. Zhang), [qwli2007@sinano.ac.cn](mailto:qwli2007@sinano.ac.cn) (Q. Li).

<sup>1</sup> These authors contributed equally to this work.

[20–23]. The limitation is that the nano-photocatalysts will only generate on the substrate surface, generally suppressing photoactive component loading at a high level, thereby resulting in very little active material available to photoexcitation and pollutant trapping [24]. Alternatively, nanoarchitecture photoelectrodes have been manufactured by anchoring photocatalytic materials onto rough conducting skeletons, including carbon felt, carbon cloth and carbon paper [25–27]. Such roughness-assisted immobilization procedure could make a strong coupling of photocatalysts onto conductive substrates, and meanwhile elevate photocatalyst loading at a certain extent [28,29]. However, the loading of photoactive materials remains far inferior to what one might expect in PFC devices because of the configuration limitation of current collectors (e.g., low surface area of photocatalyst coupling and small thickness), which is detrimental to high-performance photoelectric conversion of pollutants. A significant improvement to photoactive component loading and photoelectrode microstructure has been made by utilizing porous and high-surface-area 3D aerogels (e.g., Ni foam, Cu foam and carbon foam) as conducting skeletons for growth of nanoscale photocatalysts with various well-defined shapes [30–33], but transportation and trapping of pollutants as well as spreading and absorption of light are limited yet owing to randomly arranged channels in the 3D interconnected networks, which is particularly problematic for the photoelectrodes with large thickness and high loading of photoactive materials. Very recently, with blue  $\text{TiO}_2$  nanotube arrays and Cu-Co- $\text{WO}_3$  as anode and cathode respectively, a visible-light-driven PFC/peroxymonosulfate system has been fabricated for pollutant removal and electricity generation in real seawater [5]. Despite exciting advance of PFC made toward seawater pollutants, the expected massive pollutant trapping and high level of light absorption are still unsatisfactory due to the limited photoactive component loading on the substrate surface, which may hamper high-efficiency removal and photoelectric conversion of seawater pollutants. Consequently, exploring and achieving a rational photoelectrode structure for PFCs to simultaneously meet highly efficient seawater pollutant trapping, remarkable light absorption, as well as facile and scalable manufacturing, is highly desirable yet greatly challenging thus far.

The extrusion-based 3D printing, as a typical additive manufacturing technique, can directly construct multifarious delicate and sophisticated architectures in a highly adjustable and scalable manner [34–39]. With graphene oxide (GO) as dominant ink component, diverse multifunctional graphene-based hybridization patterns, including mesh, interdigitation and microlattice architectures, have been printed out for meeting the requirements of various applications as expected [40–44]. These findings suggest that the 3D-printed graphene structures might serve as suitable scaffolds for PFCs. Proving this hypothesis, with  $\text{TiO}_2$  as model photocatalytic material and a highly interconnected graphene network framework as current collector, a 3D-printed photoelectrode was scalably manufactured in a layer-by-layer building manner. The resulting photoelectrode featured enriched hierarchical and open pores, guaranteeing unimpeded channels for rapid pollutant diffusion throughout the entire electrode, and meanwhile affording sufficient binding sites for trapping seawater pollutants. The porous microlattice structure with uniform distribution of  $\text{TiO}_2$  nanoparticles and abundant oriented microchannels along the transversal and perpendicular directions facilitated incident light into the electrode interior, thus enabling a high light absorption to generate ample photoexcited hole-electron pairs. As a result, the integrated PFC device based on 3D-printed photoelectrode demonstrated its prominent photoelectric conversion capability for seawater pollutants, and displayed superior long-term cycle stability and self-floating behavior.

## 2. Experimental

### 2.1. Preparation of GO- $\text{TiO}_2$ ink

Aqueous GO solution was prepared from natural graphite flakes

according to the modified Hummer's method [45–48], and then freeze-dried into GO powder at  $-45^\circ\text{C}$  under vacuum (0.1 Pa). 45 g of GO powder was homogeneously dispersed into 1000 mL of deionized water, followed by mixing with proper amount of anatase  $\text{TiO}_2$  nanoparticles under vigorous stirring for 2 h, eventually yielding uniform GO- $\text{TiO}_2$  inks with different mass fractions of  $\text{TiO}_2$  in the GO- $\text{TiO}_2$  (10%, 20%, 30% and 40%).

### 2.2. 3D printing of graphene- $\text{TiO}_2$ photoanode

GO- $\text{TiO}_2$  ink was loaded into a tapered nozzle (350  $\mu\text{m}$  inner diameter) via a syringe pump with extruding rate kept at  $0.2\text{ mL min}^{-1}$ , and printed through a modified program-controlled 3D printer (Fisnar F4200n) with a constant printing speed of  $3\text{ mm s}^{-1}$  to pattern photoanode into a cubic microlattice with multiple orthogonal layers of parallel cylindrical rods on a glass substrate. After that, the 3D-printed structure was freeze dried for 24 h in vacuum, then subjected to a chemical reduction process in 55% HI acid at  $90^\circ\text{C}$  for 9 h, eventually achieving 3D graphene- $\text{TiO}_2$  photoanode. Various sophisticated 2D geometric patterns were also printed by the similar procedure, with the absence of a layer-by-layer sequence. For comparison, non-printed graphene- $\text{TiO}_2$  photoanode was also prepared by the same inks and freeze drying/HI reduction procedures.

### 2.3. Assembly of integrated self-floating PFC

A spinning solution of 12 wt% poly(vinylidene fluoride) (PVDF) in acetone/dimethylformamide (1:4, v/v) was prepared under room temperature with constant stirring for 10 h, and then transferred to five syringes (10 mL) equipped with blunt metal needles (0.4 mm in diameter), which moved periodically at a speed of  $50\text{ cm min}^{-1}$ . A DXES-3 spinning machine (SOF Nanotechnology Co., Ltd., China) was utilized for electrospinning PVDF solution, with feeding rate of  $0.8\text{ mL h}^{-1}$ , a voltage of 25 kV and needle tip-collector distance of 20 cm. The as-prepared PVDF nanofiber membrane was deposited on an aluminum foil covered roller, and then uniformly coated by Au for 5 min via magnetron sputtering technique. The resulting Au-PVDF cathode was in situ electrospun for 100 s by the above procedure to form PVDF fibrous separator, followed by assembling with 3D graphene- $\text{TiO}_2$  photoanode in a face-to-face manner, finally acquiring graphene- $\text{TiO}_2$  @PVDF@Au-PVDF PFCs with 1, 2 and 3 mm in photoanode thickness.

### 2.4. Characterization

Scanning electron microscopy (SEM) and energy-dispersive spectrometry (EDS) images were taken on a FEI Apreo C HiVac field emission scanning electron microscopy at 15 kV. X-ray diffraction (XRD) pattern data were acquired from a Bruker AXS D8 Advance X-ray diffractometer with a Cu  $\text{K}\alpha$  radiation source. Raman spectra were performed by a RM3000 Raman spectrometer with a 633 nm laser source. UV–vis diffuse reflectance spectra (DRS) were collected on a Hitachi U-4100 spectrophotometer with  $\text{BaSO}_4$  as a reflectance reference. The rheological properties of inks were analyzed using a HAAKE RS 6000 rheometer, including viscosity versus shear rate ( $1\text{--}100\text{ s}^{-1}$ ) and preservation time (4 weeks), as well as storage modulus ( $G'$ ) and loss modulus ( $G''$ ) versus shear stress (0.1–1000 Pa) and frequency (0.1–100 Hz).

### 2.5. Measurements

Electrochemical and photoelectrochemical measurements were conducted on a PGSTAT302N electrochemical workstation. Photocurrent response was tested in the simulated seawater at the bias potential of 0 V. Polarization curves were obtained by galvanodynamic measurements ( $0.5\text{ }\mu\text{A s}^{-1}$ ). Electrochemical impedance spectroscopy (EIS) was carried out at an AC amplitude of 5 mV from 0.01 to  $10^5\text{ Hz}$ . Linear sweep voltammogram (LSV) was performed in a standard three-

electrode system with graphene-TiO<sub>2</sub> photoanode or Au-PVDF cathode as working electrode, Ag/AgCl and Pt wire as the reference and counter electrode, respectively. A 300 W Xe lamp with a bandpass filter of 420–800 nm was used as radiation source (100 mW cm<sup>-2</sup>). The solar flux was tested via an optical power meter (CEL-NP2000–2A). The amount of n-hexane in the seawater was analyzed by a gas chromatograph (GC-2014, Shimadzu Corp.). The Cl<sup>-</sup> concentration was determined by ion chromatography (ICS 2000, Dionex). The pH of the seawater was measured by a pH meter (PHS-3 C). The simulated seawater used throughout this study, containing Na<sup>+</sup> (10.7 g L<sup>-1</sup>), Mg<sup>2+</sup> (1.3 g L<sup>-1</sup>), K<sup>+</sup> (0.4 g L<sup>-1</sup>), Ca<sup>2+</sup> (0.5 g L<sup>-1</sup>) and Cl<sup>-</sup> (18.9 g L<sup>-1</sup>) was prepared, followed by adding n-hexane or other pollutants (diesel, gasoline, cyclohexane, n-pentane and neopentane) to yield polluted seawater.

### 3. Results and discussion

#### 3.1. Design of integrated self-floating seawater pollutant-fed PFC

The conceptual design of integrated self-floating PFC for simultaneous degradation and electricity generation of seawater pollutant by utilizing full-spectrum solar irradiance was schematically illustrated in Fig. 1. 3D graphene-TiO<sub>2</sub> aerogel microlattice at the top, porous Au-PVDF layer at the bottom and thin yet porous PVDF interlayer sandwiched in between were served as photoanode, cathode and separator, respectively, and assembled into an integrated self-floating device, where 0D TiO<sub>2</sub> nanoparticles acting as photosensitive material were uniformly attached onto hierarchically porous conductive skeleton built by 2D graphene nanosheets. The integrated device by tight connection of separator to the top and bottom electrodes endowed it high structure stability for self-floating operation in the polluted seawater systems. The 3D porous structure offered the abundant micro- and nanochannels along the transversal and perpendicular directions of device, favoring continuous supply of seawater pollutant from all directions to the photoanode, which made it possible for persistent electricity generation. The enriched hierarchical pores of self-floating photoanode with

interconnected conductive network could significantly facilitate the incident light into the electrode interior when exposed under solar irradiation, thus enabling a high light absorption. Meanwhile, the numerous open pores originated from random-aligned graphene sheets furnished sufficient surface area for easily trapping seawater pollutant. The above merits contributed to a systematic optimization of pollutant transportation and trapping, light absorption and stable structure. A plausible photoelectric mechanism of PFC for seawater pollutant could be described as follows. Upon full-spectrum solar irradiation, TiO<sub>2</sub> attached onto graphene nanosheet was excited to generate ample electron-hole pairs. In view of a lower Fermi level and superior electrical conductivity of graphene nanosheet compared to TiO<sub>2</sub>, the photo-generated electrons were quickly transferred from TiO<sub>2</sub> conduction band towards graphene nanosheet and then to the cathode via an external circuit, effectively impeding the recombination of electrons and holes, thereby enabling numerous holes with significant oxidizing power on the photoanode to oxidize pollutant into CO<sub>2</sub>, which would greatly improve the degradation efficiency and electricity generation of seawater pollutant adsorbed to the photoanode. Consequently, a sustaining and highly efficient electricity generation in polluted seawater could be expected by the integrated self-floating PFC device, opening up new opportunities of photocatalytic system for addressing the seawater-energy nexus.

#### 3.2. 3D printing and characterization of aerogel photoanode

3D graphene-TiO<sub>2</sub> aerogel was scalably manufactured via the direct ink writing strategy using GO-TiO<sub>2</sub> ink, as schematically illustrated in Fig. 2a. To enable a smooth 3D printing of aerogel electrodes and favorable shape maintenance of printed structures targeting high-performance devices, the rheological properties of inks remained key. As evidenced in Fig. 2b, the viscosity of all inks featured a nearly linear decrease with the increase of shear stress from 1 to 100 s<sup>-1</sup>, reflecting typical shear-thinning non-Newtonian fluid behavior and highly adjustable viscosity, which could enable printable inks to flow continuously through a fine nozzle upon extrusion. A favorable self-supporting

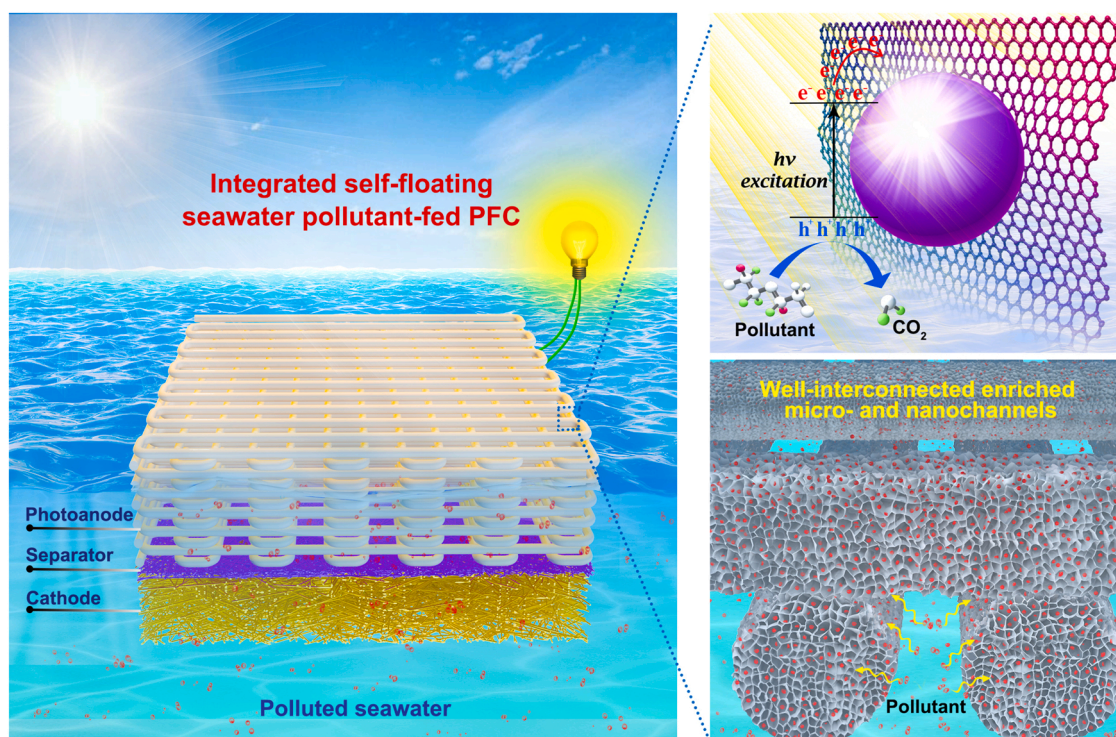
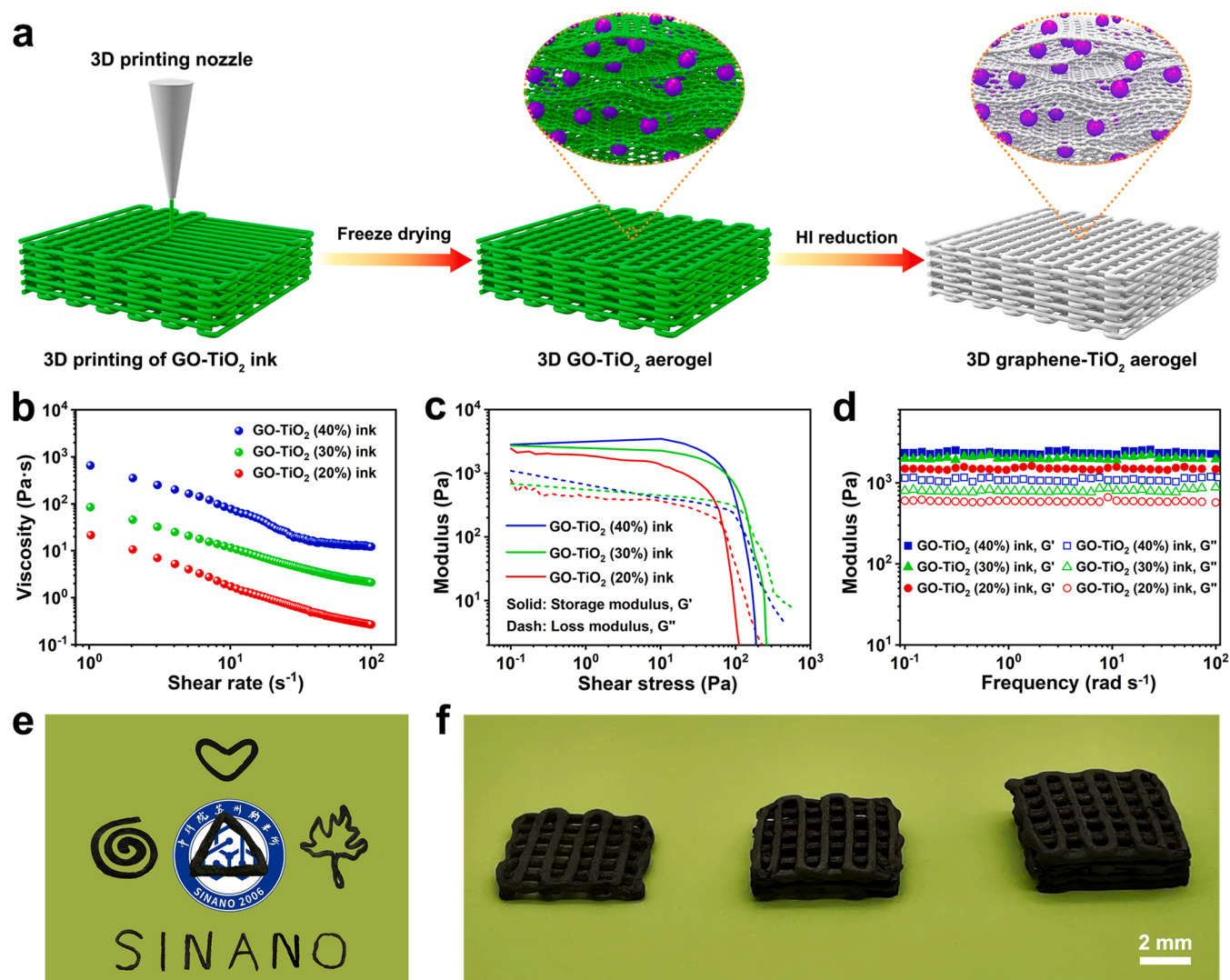


Fig. 1. Structure design of integrated self-floating PFC for concurrent seawater pollutant degradation and electricity generation.





**Fig. 2.** Fabrication procedure and ink rheological behaviors. (a) Schematic of the fabrication process of 3D graphene-TiO<sub>2</sub> aerogel. (b) Viscosity as a function of shear rate for various GO-TiO<sub>2</sub> inks. Storage modulus ( $G'$ ) and loss modulus ( $G''$ ) as functions of (c) shear stress and (d) frequency for various GO-TiO<sub>2</sub> inks. Optical images of 3D-printed graphene-TiO<sub>2</sub> aerogels in (e) various 2D geometric patterns and (f) 3D microlattices with varying thickness.

behavior of inks loaded in the inverted glass bottles over 72 h further revealed excellent printability to get stable architectures without collapse (Fig. S1). Moreover, the ink viscosity remained almost unchanged within four weeks (Fig. S2), manifesting that the ink system held favorable stability and was suitable for long-term storage. Fig. 2c displays the storage modulus ( $G'$ ) and loss modulus ( $G''$ ) of GO-TiO<sub>2</sub> inks with different amount of TiO<sub>2</sub> as a function of shear stress. Inks featured predominantly solid-like behavior with higher  $G'$  than  $G''$  before reaching the yielding stress, facilitating the solidification of ink during 3D printing. After the yield point, the  $G'$  dropped dramatically and eventually surpassed the  $G''$ , manifesting liquid-like behavior in viscoelastic materials. As further validated by the dynamic modulus vary with frequency,  $G'$  values of all inks were distinctly larger than those of their corresponding  $G''$  within the entire frequency interval tested (Fig. 2d). These prominent rheological characteristics ensured that the homogeneous hybrid ink could be extruded fluently from micrometer-sized nozzles, and then kept cylindrical shape once "set" in the air with narrow deviations in filament thickness throughout 20 stacked layers (Fig. S3), proving relatively high printed structural accuracy and superior shape stability. The freestanding GO-TiO<sub>2</sub> microlattice printed in a layer-by-layer building manner was freeze-dried to remove water and turn into aerogel with interior structure still integrally maintained,

followed by chemical reduction with HI acid to finally generate 3D graphene-TiO<sub>2</sub> aerogel with regular multiscale pore architecture, in which photoactive TiO<sub>2</sub> nanoparticles were homogeneously distributed and anchored onto graphene nanosheets as conductive supporting skeleton. As expected, regular microlattice architecture with varying thickness could be successfully constructed, and various sophisticated patterns could also be easily printed, such as heart, spiral, triangular, leaf and "SINANO" (Fig. 2e,f).

The structural characteristics of 3D-printed aerogel photoanode were illuminated through SEM. Top-view SEM images evidently exhibited highly uniform and well-defined square pores (ca. 500  $\mu$ m) built by continuous and tight stack of multiple orthogonal layers of parallel cylindrical filaments with ca. 360  $\mu$ m in diameter (Fig. 3a-c), and demonstrated abundant pores originated from wrinkled and randomly oriented sheets on the filament surface, with pore size ranging from hundreds of nanometers to tens of micrometers (Fig. 3d). A typical cross-sectional SEM image of aerogel photoanode displayed that the filament at junction was intimately welded together without collapse (Fig. 3e,f), which would be conducive to the structural stability, formation of conductive network and continuous supply of seawater pollutant from all directions to the photoanode. A close observation of cross section revealed an interconnected porous configuration with high TiO<sub>2</sub>



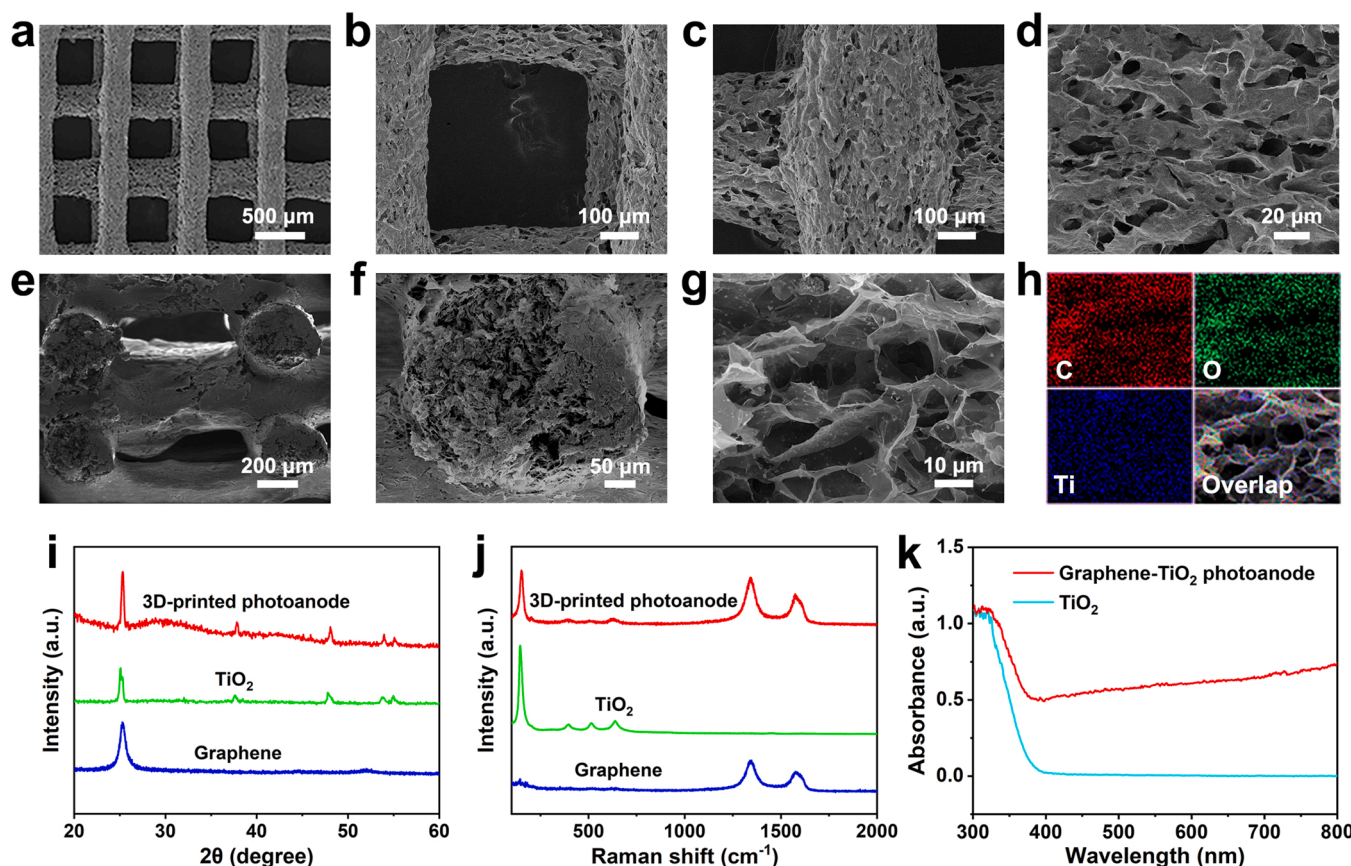


**Fig. 3.** Morphological, compositional and light-absorbing characterizations of 3D-printed aerogel photoanode with mass loading of 40%  $\text{TiO}_2$ . (a) Top-view SEM image and (b-d) its magnification. (e) Cross-sectional SEM image and (f,g) its magnification. (h) EDS element mappings of C, O and Ti corresponding to Fig. 3g. (i) XRD patterns and (j) Raman spectra of graphene,  $\text{TiO}_2$  and 3D-printed photoanode. (k) UV-vis DRS of  $\text{TiO}_2$  and 3D-printed graphene- $\text{TiO}_2$  photoanode.

nanoparticle loading (Fig. 3g), as further testified by EDS element mappings, with uniform distribution of C, O and Ti elements throughout the filament (Fig. 3h). These observations confirmed that the 3D-printed aerogel photoanode featured enriched hierarchical and open pores with uniform distribution of  $\text{TiO}_2$  nanoparticles, not only facilitating incident light into the electrode interior and its effective absorption to generate ample photoexcited hole-electron pairs, but also affording sufficient binding sites for trapping seawater pollutant to generate electricity persistently upon full-spectrum solar irradiation when served as PFC in polluted seawater. The composition of 3D-printed photoanode was examined using XRD and Raman spectra, in which all characteristic peaks of graphene and anatase  $\text{TiO}_2$  appeared as expected (Fig. 3i,j), adequately demonstrating that anatase  $\text{TiO}_2$  nanoparticles were successfully combined with graphene sheets to form the PFC photoanode. UV-vis DRS analyses clearly identified that the 3D-printed graphene- $\text{TiO}_2$  photoanode featured significantly enhanced light absorbance compared to pure anatase  $\text{TiO}_2$ , especially within visible light range (Fig. 3k), reflecting exceptional visible-light harvesting capacity and charge carrier generation of the resultant photoanode, which would make it practical PFC for highly efficient degradation and electricity generation of seawater pollutant under solar irradiation.

### 3.3. Assembly procedure and performance assessment of PFC system

Fig. 4a schematically illustrates the fabrication process of an integrated self-floating PFC for efficient seawater pollutant degradation and synchronous electricity generation. The PVDF layer with multiscale pores from macro to micro levels was prepared by depositing electrospun PVDF nanofibers with ca. 500 nm in diameter onto a metal substrate (Fig. S4), followed by magnetron sputtering to achieve uniform Au

wrapping of PVDF nanofibers without significant shift in pore size (Fig. S5). The resulting conductive Au-PVDF layer served as cathode, and was tightly welded to electrospun PVDF fibrous separator with thin thickness and high porosity (Fig. 4b). After assembling onto photoanode with ample open and hierarchical pores, the graphene- $\text{TiO}_2$  filaments, PVDF and Au-PVDF fibers were entangled layer-by-layer in the interfacial region (Fig. 4c), adequately proving excellent bonding within the trilayers and well-interconnected multibranched macro-, micron-, and sub-micron-sized channels of the trilayer, which would contribute to stable structure of the constructed PFC and minimize the seawater pollutant transport resistance from bulk seawater to photoanode. Strikingly, the as-fabricated graphene- $\text{TiO}_2$  @PVDF@Au-PVDF PFC could overcome gravity and achieve long-term floating stability with its upper surface approximately parallel to the horizontal plane (Fig. 4d), owing to its highly porous structure and surface tension in seawater originated from hydrophobic PVDF and graphene components in PFC, thereby enabling high light absorption under solar irradiation and potentially easy deployment in large-scale solar seawater-energy conversion. EIS analysis of PFC exhibited that the impedance under simulated sunlight irradiation was lower than that in the dark (Fig. 4e), signifying a more efficient charge transfer during operation. LSV curves revealed that under dark and simulated sunlight, the light irradiation initiated an evidently elevated current of photoanode compared to the dark, and a nearly overlapping variation tendency of cathode was observed under two conditions (Fig. S6), reflecting excellent activity of photoanode under visible light irradiation, which was further verified by its stable photocurrent response without noticeable decline after 240 min irradiation (Fig. S7). Fig. 4f displays the transient photocurrent density of PFC in light on/off cycles under simulated sunlight irradiation. A photocurrent density at a milliampere level was instantly

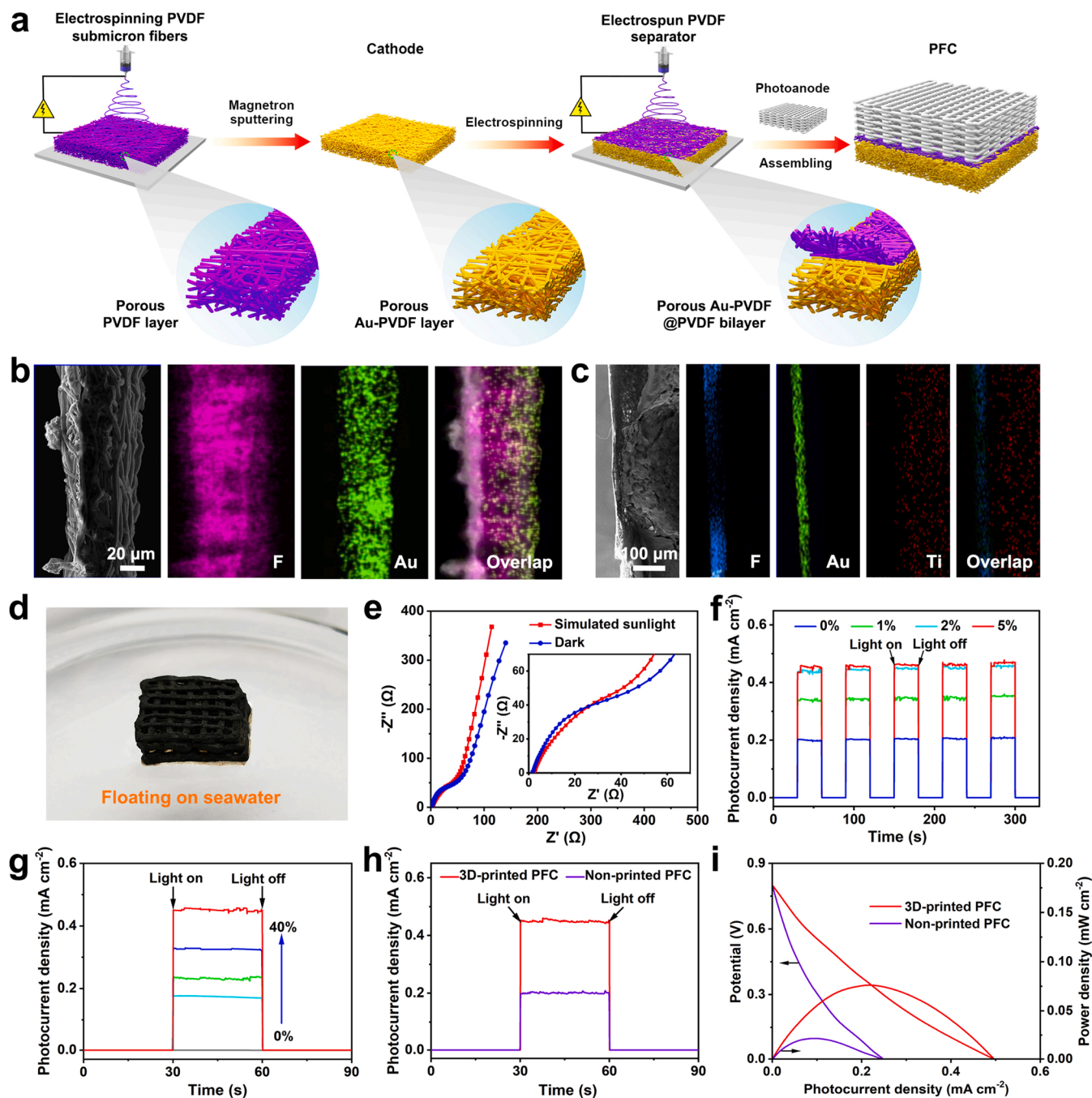


**Fig. 4.** Fabrication and characterization of integrated 3D-printed graphene-TiO<sub>2</sub> @PVDF@Au-PVDF PFC. (a) Schematic of preparation process. (b) Cross-sectional SEM image of Au-PVDF@PVDF and its corresponding elemental mappings of F and Au. (c) Cross-sectional SEM image and corresponding elemental mappings of F, Au and Ti at the electrode-separator interface. (d) Photograph of printed PFC floating on seawater. (e) Nyquist plots under dark and simulated sunlight. (f) Photocurrent response in n-hexane solutions with different concentration under simulated sunlight. (g) Photocurrent response of printed PFC with different weight percentages of TiO<sub>2</sub> in photoanode. Photocurrent response (h) and polarization/power curves (i) of 3D-printed and non-printed PFCs.

generated in seawater without n-hexane, and significantly increased following the elevation of n-hexane concentration ranging from 1 wt% to 2 wt%, owing to the adsorption of more n-hexane molecules at higher substrate concentration. Note that with further increase of n-hexane concentration to 5 wt%, the photocurrent featured a slight enhancement originated from the restriction of binding sites involved. When the concentration of substrate was overloaded, the binding sites became saturated with n-hexane molecules under such n-hexane solution conditions and no more n-hexane could be absorbed by the photoanode. Photocurrent response as a function of n-hexane concentration testified that n-hexane in seawater could be efficiently converted into electric

energy under simulated sunlight. For comparison, the photocurrent response in pure water containing n-hexane was also conducted (Fig. S8). A near-zero photocurrent density implied that electricity generation of n-hexane hardly occurred in the water without ions. The photocurrent response of PFC with different weight percentages of TiO<sub>2</sub> in photoanode were examined to elucidate the effect of TiO<sub>2</sub>. As envisioned in Fig. 4 g, no obvious photocurrent response could be observed at the absence of TiO<sub>2</sub> owing to the unavailable photoexcitation under visible light irradiation. The photocurrent density featured a distinct enhancement with the increasing TiO<sub>2</sub> content up to 40%, manifesting that the TiO<sub>2</sub> was highly effective in improving the photoelectric

conversion of seawater pollutants, which was believed to be closely related to its existing state in the photoanode. The higher the content of  $\text{TiO}_2$ , the better the transmittance of photoanode, resulting in the more excited  $\text{TiO}_2$  nanoparticles at the near surface and in the interior of photoanode, thereby yielding a higher photocurrent. To better illuminate the role of 3D printing in fabricating PFC, non-printed graphene- $\text{TiO}_2$  photoanode with the same size and  $\text{TiO}_2$  content to the printed photoanode was also prepared for comparison (Fig. S9), and the corresponding photocurrent response, polarization and power curves of two assembled PFCs were collected in the seawater containing 2% n-hexane under simulated sunlight irradiation (Fig. 4 h,i). Strikingly, the PFC assembled by 3D-printed photoanode demonstrated its exceptional electricity generation performance for seawater pollutants as expected, with photocurrent density of  $0.45 \text{ mA cm}^{-2}$  and power density of  $0.07 \text{ mW cm}^{-2}$ , 2.2 and 3.5 times higher than that achieved by the PFC based on non-printed photoanode owing to the superior pollutant trapping and light absorption enabled by 3D-printed photoanode architecture with well-interconnected hierarchical channels, adequately proving that 3D printing was an effective strategy for manufacturing high-performance PFCs. Additionally, note that the photocurrent response of 3D-printed PFC to n-hexane in seawater increased with photoanode thickness up to 2 mm owing to sufficient light absorption and more binding sites of n-hexane, and subsequently declined at larger photoanode thickness, which could be mainly ascribed to limited

degradation of n-hexane aggregated onto photoanode (Fig. S10 and Fig. S11).

Polarization and power density curves were collected to appraise the photovoltaic performance of this 3D-printed PFC in the seawater with 1% n-hexane. Upon simulated sunlight irradiation, this PFC yielded a short-circuit photocurrent density of ca.  $0.41 \text{ mA cm}^{-2}$  and a maximum output power density of ca.  $0.06 \text{ mW cm}^{-2}$ , significantly higher than that generated in the dark (Fig. S12), proving that simulated sunlight could effectively boost the photovoltaic performance of PFC for electricity generation using seawater pollutant as a substrate. Besides, the photovoltaic properties of the printed PFC were also conducted in the seawaters with different concentration of n-hexane. The polarization curves revealed that the short-circuit photocurrent density elevated with the increasing n-hexane concentration from 1% to 5% (Fig. 5a), and the corresponding power curves demonstrated considerable output power densities (Fig. 5b). The maximum power density, short-circuit current density and open circuit voltage reached as high as  $0.09 \text{ mW cm}^{-2}$ ,  $0.53 \text{ mA cm}^{-2}$  and  $0.8 \text{ V}$ , respectively, which compared favorably with other state-of-the-art PFCs reported previously (Table S1), further confirming the powerful capability of our PFC for highly efficient electricity generation of seawater pollutants. Remarkably, the printed PFC also demonstrated its exceptional stability in solar seawater-energy conversion as expected, with well-maintained I-t curve and structure feature after 200 switch on-off cycles of xenon light (Fig. 5c, Fig. S13), and

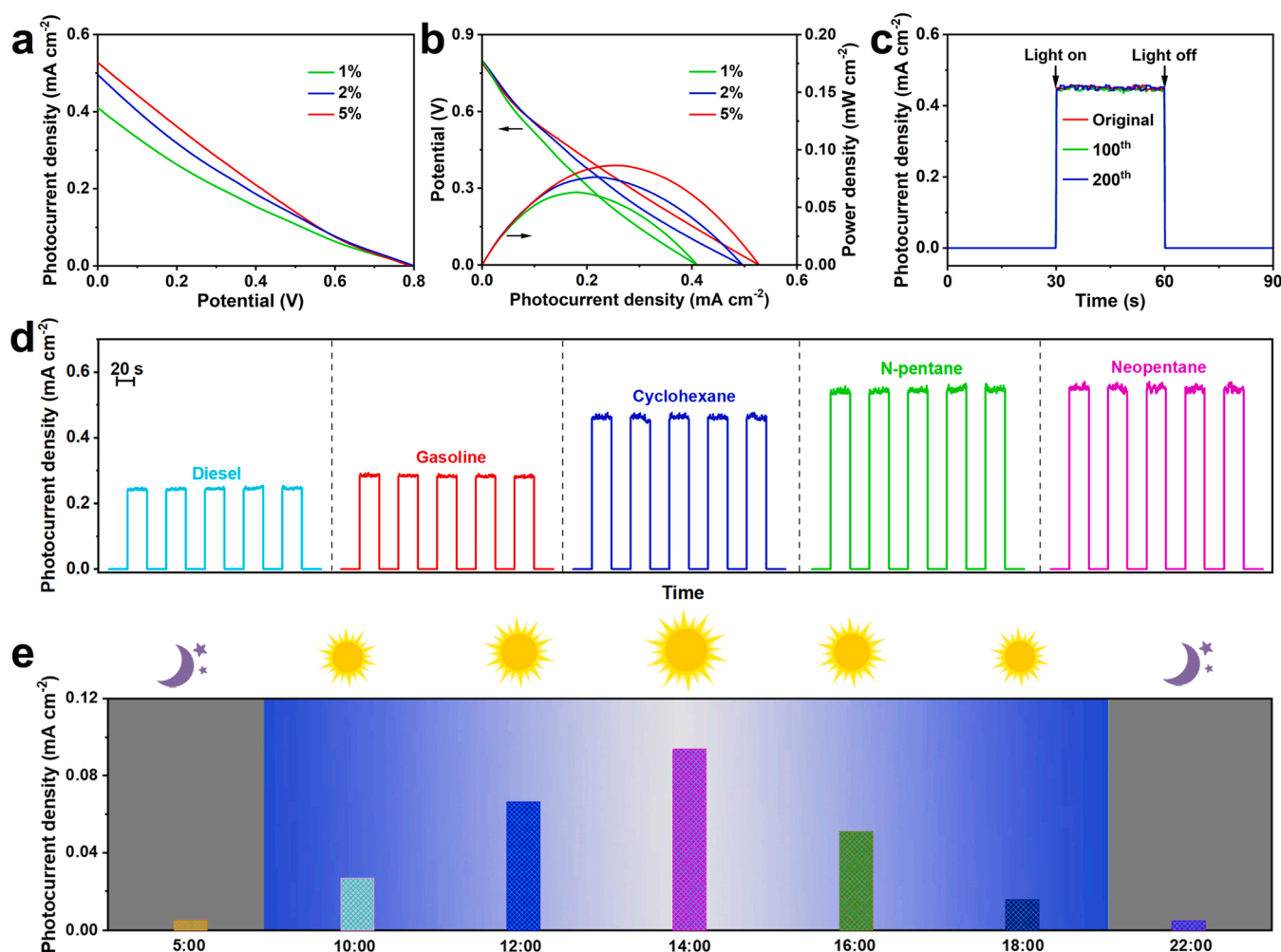


**Fig. 5.** Electricity generation performance of the 3D-printed PFC for seawater pollutants. (a) Polarization curves and (b) corresponding power density curves in the seawaters with different concentration of n-hexane under simulated sunlight irradiation. Photocurrent response for (c) various cycles in the seawater with 2% n-hexane and (d) other seawater pollutants under simulated sunlight irradiation. (e) Photocurrent response in the seawater with 2% n-hexane at diverse time on a sunny day.



almost unchanged photocurrent after a 60-day storage period at ambient conditions (Fig. S14), which would be propitious to its practical applications. Upon light irradiation for 100 min, five successive measurements presented that the degradation efficiencies of n-hexane in the seawater held at a high level with the value ranging from 92.4% to 90.3% (Fig. S15), further reflecting extraordinary reusability of PFC system and its powerful ability of pollutant removal. Additionally, note that during the visible-photocatalytic degradation and electricity generation of n-hexane, the  $\text{Cl}^-$  concentration and pH value in the simulated seawater kept almost unchanged to the irradiation time (Fig. S16), suggesting that  $\text{Cl}^-$  reaction and basic hydroxide formation hardly occurred in the as-constructed PFC system. Fig. 5d presents the time-dependent photocurrent response of printed PFC toward various seawater pollutants including diesel, gasoline, cyclohexane, n-pentane and neopentane, which feature an inherently good affinity to graphene in the photoanode. Upon simulated sunlight irradiation, the photocurrent was generated within 0.1 s for all samples, suggesting a quick response time. The approximate and relatively low photocurrent densities with a tiny shift from 0.24 to 0.27  $\text{mA cm}^{-2}$  were observed for diesel and gasoline, which could be related to their intrinsic composite state consisting largely of longer carbon chain hydrocarbons, inevitably hampering their infiltration and adsorption within the photoanode. By contrast, a significantly enhanced photocurrent response appeared as expected for cyclohexane, n-pentane and neopentane with shorter carbon chains owing to their ready diffusion into the interior of photoanode, with the photocurrent densities up to 0.49, 0.56 and 0.57  $\text{mA cm}^{-2}$ , respectively. Apparently, the chain-typed n-pentane and neopentane with the same molecular weights displayed a nearly equal photocurrent density, slightly higher than that toward higher molecular weight cyclohexane, which might be attributed to the limitation of adsorption density originated from larger size and steric hindrance of cyclohexane. These findings implied the potential ability of the as-fabricated PFC to effectively generate power from multiple seawater pollutants, as was further validated by polarization curve tests with favorable output power density and short-circuit current (Fig. S17). Fig. 5e displays the photocurrent response of printed PFC for seawater pollutants in real-world situations, where the outdoor solar flux in the range of ca. 3–71  $\text{mW cm}^{-2}$  was recorded from 5:00–22:00 on a sunny day (Fig. S18). The photocurrent varied with time, reached the maximum at 14:00, and could still be available even under the moonlight, signifying the practical feasibility of the proposed PFC.

#### 4. Conclusion

In summary, for the first time, we demonstrated the capability of an extrusion-based 3D printing for constructing rational photoelectrode architectures in a facile, efficient, controllable and scalable way. The resulting 3D-printed microlattice photoelectrode featured well-interconnected oriented channels as well as enriched hierarchical and open pores built by graphene sheets with uniform loading of  $\text{TiO}_2$  nanoparticles, thereby facilitating the light spreading and absorption to generate ample photoexcited hole-electron pairs, and meanwhile guaranteeing unimpeded channels and sufficient binding sites for highly efficient transportation and trapping of seawater pollutants. Benefiting from the special architecture, the integrated PFC demonstrated eminent photoelectric conversion capability for seawater pollutants, with a high open circuit voltage of 0.8 V, a short circuit current density of 0.53  $\text{mA cm}^{-2}$  and a maximum power density of 0.09  $\text{mW cm}^{-2}$ , while maintaining superior self-floating behavior and cycling stability over 200 cycles. The as-constructed self-floating PFC would be highly promising for marine pollution control, involving the sustainable degradation and electricity generation of various marine pollutants (e.g., hydrocarbons, dyes and pesticides) under sunlight irradiation.

#### CRediT authorship contribution statement

**Zhengpeng Yang:** Conceptualization, Investigation, Writing – review & editing. **Xinyin Yang:** Investigation, Formal analysis, Writing – original draft. **Meng Zhu:** Investigation, Data curation, Methodology. **Yutao Niu:** Formal analysis, Software. **Chunjing Zhang:** Methodology, Formal analysis. **Ping Li:** Methodology. **Yongyi Zhang:** Conceptualization, Funding acquisition, Writing – review & editing. **Zhichao Xu:** Resources. **Qingwen Li:** Supervision, Funding acquisition, Writing – review & editing.

#### Declaration of Competing Interest

The authors declare that they have no known competing financial interests or personal relationships that could have appeared to influence the work reported in this paper.

#### Data availability

Data will be made available on request.

#### Acknowledgements

Z. Yang, X. Yang and M. Zhu contributed equally to this work. The authors are grateful to the financial supports from the National Natural Science Foundation of China (52062048, 52103290), the Science and Technology Project of Jiangxi Province (20192BCD40017), Jiangxi Double Thousand Talent Program (S2018LQCQ0016, Y. Zhang) and the Science and Technology Project of Nanchang, China (2017-SJSYS-008).

#### Appendix A. Supporting information

Supplementary data associated with this article can be found in the online version at doi:10.1016/j.apcatb.2023.122646.

#### References

- [1] F.Y. Chen, J.H. Li, L.G. Xia, J.C. Wang, S. Chen, Y. Zhang, J. Bai, L. Linsen, T. S. Zhou, M. Rahim, Q.J. Xu, B.X. Zhou, The synergic generation of  $\text{CO}_3^{\cdot-}$  and  $\text{O}_2^{\cdot-}$  radicals in a novel photocatalytic fuel cell for efficient oxidation of carbonate-containing wastewater and simultaneous electricity production, *Appl. Catal. B Environ.* 277 (2020), 119227, <https://doi.org/10.1016/j.apcatb.2020.119227>.
- [2] M.J. Qiu, P. Sun, G.F. Cui, Y.X. Tong, W.J. Mai, A flexible microsupercapacitor with integral photocatalytic fuel cell for self-charging, *ACS Nano* 13 (2019) 8246–8255, <https://doi.org/10.1021/acsnano.9b03603>.
- [3] X.Y. Chen, J.J. Yao, B. Xia, J.Y. Gan, N.Y. Gao, Z. Zhang, Influence of pH and DO on the ofloxacin degradation in water by UVA-LED/ $\text{TiO}_2$  nanotube arrays photocatalytic fuel cell: mechanism, ROSs contribution and power generation, *J. Hazard. Mater.* 383 (2020), 121220, <https://doi.org/10.1016/j.jhazmat.2019.121220>.
- [4] Z.P. Yang, M. Zhu, Y.T. Niu, E. Kozliak, B. Yao, Y.Y. Zhang, C.J. Zhang, T.T. Qin, Y. H. Jia, Q.W. Li, A graphene-based coaxial fibrous photofuel cell powered by mine gas, *Adv. Funct. Mater.* 29 (2019), 1906813, <https://doi.org/10.1002/adfm.201906813>.
- [5] J.Q. Sun, L.F. Liu, F.L. Yang, A visible-light-driven photocatalytic fuel cell/peroxymonosulfate (PFC/PMS) system using blue  $\text{TiO}_2$  nanotube arrays (TNA) anode and Cu-Co- $\text{WO}_3$  cathode for enhanced oxidation of organic pollutant and ammonium nitrogen in real seawater, *Appl. Catal. B Environ.* 308 (2022), 121215, <https://doi.org/10.1016/j.apcatb.2022.121215>.
- [6] M. Zhang, Z.Z. Zhang, Y.H. Xu, Z.R. Wen, C.F. Ding, Y.S. Guo, K. Wang, A novel self-powered aptasensor for digoxin monitoring based on the dual-photoelectrode membrane/mediator-free photofuel cell, *Biosens. Bioelectron.* 156 (2020), 112135, <https://doi.org/10.1016/j.bios.2020.112135>.
- [7] X.J. Du, D. Jiang, Q. Liu, N. Hao, K. Wang, Ingenious dual-photoelectrode internal-driven self-powered sensing platform for the power generation and simultaneous microcystin monitoring based on the membrane/mediator-free photofuel cell, *Anal. Chem.* 91 (2019) 1728–1732, <https://doi.org/10.1021/acs.analchem.8b05509>.
- [8] Q.Y. Zeng, J. Bai, J.H. Li, L.S. Li, L.G. Xia, B.X. Zhou, Y.G. Sun, Highly-stable and efficient photocatalytic fuel cell based on an epitaxial  $\text{TiO}_2/\text{WO}_3/\text{W}$  nanothorn photoanode and enhanced radical reactions for simultaneous electricity production and wastewater treatment, *Appl. Energy* 220 (2018) 127–137, <https://doi.org/10.1016/j.apenergy.2018.03.042>.
- [9] L.L. Hu, Y.H. Liao, D.H. Xia, F. Peng, L. Tan, S.Y. Hu, C.S. Zheng, X.L. Lu, C. He, D. Shu, Engineered photocatalytic fuel cell with oxygen vacancies-rich rGO/

- BiO<sub>1-x</sub>I as photoanode and biomass-derived N-doped carbon as cathode: promotion of reactive oxygen species production via Fe<sup>2+</sup>/Fe<sup>3+</sup> redox, *Chem. Eng. J.* 385 (2020), 123824, <https://doi.org/10.1016/j.cej.2019.123824>.
- [10] S.L. Shinde, S. Ishii, T.D. Dao, R.P. Sugavaneshwar, T. Takei, K.K. Nanda, T. Nagao, Enhanced solar light absorption and photoelectrochemical conversion using TiN nanoparticle-incorporated C<sub>3</sub>N<sub>4</sub>-C dot sheets, *ACS Appl. Mater. Interfaces* 10 (2018) 2460–2468, <https://doi.org/10.1021/acsami.7b15066>.
- [11] T.T. Yu, Q.S. Liu, Z.Y. Zhu, W.W. Wu, L.F. Liu, J.L. Zhang, C.F. Gao, T. Yang, Construction of a photocatalytic fuel cell using a novel Z-scheme MoS<sub>2</sub>/rGO/Bi<sub>2</sub>S<sub>3</sub> as electrode degraded antibiotic wastewater, *Sep. Purif. Technol.* 277 (2021), 119276, <https://doi.org/10.1016/j.seppur.2021.119276>.
- [12] Q.Y. Zeng, S. Chang, A. Beyhaqi, S.P. Lian, H.S. Xu, J.P. Xie, F. Guo, M.Q. Wang, C. Hu, Efficient solar hydrogen production coupled with organics degradation by a hybrid tandem photocatalytic fuel cell using a silicon-doped TiO<sub>2</sub> nanorod array with enhanced electronic properties, *J. Hazard. Mater.* 394 (2020), 121425, <https://doi.org/10.1016/j.jhazmat.2019.121425>.
- [13] L. Zhang, C. Liang, H. Guo, C.G. Niu, X.F. Zhao, X.J. Wen, G.M. Zeng, Construction of a high-performance photocatalytic fuel cell (PFC) based on plasmonic silver modified Cr-BiOCl nanosheets for simultaneous electricity production and pollutant removal, *Nanoscale* 11 (2019) 6662–6676, <https://doi.org/10.1039/c8nr09616c>.
- [14] X.D. An, D. Stelter, T. Keyes, B.M. Reinhard, Plasmonic photocatalysis of urea oxidation and visible-light fuel cells, *Chem* 5 (2019) 2228–2242, <https://doi.org/10.1016/j.chempr.2019.06.014>.
- [15] M.H. Li, Y.B. Liu, L.M. Dong, C.S. Shen, F. Li, M.H. Huang, C.Y. Ma, B. Yang, X. Q. An, W. Sand, Recent advances on photocatalytic fuel cell for environmental applications: the marriage of photocatalysis and fuel cells, *Sci. Total Environ.* 668 (2019) 966–978, <https://doi.org/10.1016/j.scitotenv.2019.03.071>.
- [16] J.L. Zhang, Y.H. Wang, K. Huang, K.J. Huang, H. Jiang, X.M. Wang, Enzyme-based biofuel cells for biosensors and in vivo power supply, *Nano Energy* 84 (2021), 105853, <https://doi.org/10.1016/j.nanoen.2021.105853>.
- [17] D.L. Pan, S.N. Xiao, X.F. Chen, R.P. Li, Y.N. Cao, D.Q. Zhang, S.S. Pu, Z.C. Li, G. S. Li, H.X. Li, Efficient photocatalytic fuel cell via simultaneous visible-photoelectrolytic degradation and electricity generation on a porous coral-like WO<sub>3</sub>/W photoelectrode, *Environ. Sci. Technol.* 53 (2019) 3697–3706, <https://doi.org/10.1021/acs.est.8b05685>.
- [18] Y.X. Chen, W.H. Ji, K. Yan, J. Gao, J.D. Zhang, Fuel cell-based self-powered electrochemical sensors for biochemical detection, *Nano Energy* 61 (2019) 173–193, <https://doi.org/10.1016/j.nanoen.2019.04.056>.
- [19] L.F. Plaça, P.L.S. Vital, L.E. Gomes, A.C. Roveda, D.R. Cardoso, C.A. Martins, H. Wender, Black TiO<sub>2</sub> photoanodes for direct methanol photo fuel cells, *10.1021/acsami.2c04802*, *ACS Appl. Mater. Interfaces* (2022), <https://doi.org/10.1021/acsami.2c04802>.
- [20] Y.F. Ding, J.F. Li, K. Yan, J.D. Zhang, A miniature self-powered electrochemical sensor for the determination of patulin based on an integrated photocatalytic fuel cell, *Sens. Actuators B Chem.* 369 (2022), 132259, <https://doi.org/10.1016/j.snb.2022.132259>.
- [21] B.Z. Qian, Q. Xu, Y. Wu, Y. Zhang, H. Li, Y. Wang, B.X. Wang, S. Li, X.M. Song, A highly efficient photocatalytic methanol fuel cell based on non-noble metal photoelectrodes: study on its energy band engineering via experimental and density functional theory method, *J. Power Sources* 478 (2020), 228756, <https://doi.org/10.1016/j.jpowsour.2020.228756>.
- [22] T. Parvizi, J.B. Parsa, High-efficient photocatalytic fuel cell integrated with peroxide activation for electricity production by degradation of refractory organics, *J. Power Sources* 484 (2021), 229264, <https://doi.org/10.1016/j.jpowsour.2020.229264>.
- [23] J. Zhang, S. Lv, J.L. Zheng, P.L. Yang, J. Li, X.H. Wu, T.X. Jin, C.X. Cheng, Y. W. Song, L. Li, Self-CO<sub>2</sub> recycling photocatalytic fuel cell for enhancing degradation of pollutants and production of carbon-neutral fuel, *ACS Sustain. Chem. Eng.* 8 (2020) 11133–11140, <https://doi.org/10.1021/acssuschemeng.0c01906>.
- [24] Y. He, K.D. Chen, M.K.H. Leung, Y.Z. Zhang, L. Li, G.S. Li, J. Xuan, J.F. Li, Photocatalytic fuel cell—a review, *Chem. Eng. J.* 428 (2022), 131074, <https://doi.org/10.1016/j.cej.2021.131074>.
- [25] S.H. Thor, L.N. Ho, S.A. Ong, C.Z.A. Abidin, C.Y. Heah, N. Nordin, Y.P. Ong, K. L. Yap, Advanced oxidation treatment of amaranth dye synchronized with electricity generation using carbon-based cathodes in a sustainable photocatalytic fuel cell integrated electro-fenton system, *J. Environ. Chem. Eng.* 9 (2021), 106439, <https://doi.org/10.1016/j.jece.2021.106439>.
- [26] L.N. Tang, L.F. Liu, Q.Y. Chen, F.L. Yang, X. Quan, The construction and performance of photocatalytic-fuel-cell with Fe-MoS<sub>2</sub>/reduced graphene oxide@ carbon fiber cloth and ZnFe<sub>2</sub>O<sub>4</sub>/Ag/Ag<sub>3</sub>VO<sub>4</sub>@carbon felt as photo electrodes, *Electrochim. Acta* 362 (2020), 137037, <https://doi.org/10.1016/j.electacta.2020.137037>.
- [27] J. Liu, M. Xia, R. Chen, X. Zhu, Q. Liao, D.D. Ye, B. Zhang, W. Zhang, Y.X. Yu, A membrane-less visible-light responsive micro photocatalytic fuel cell with the laterally-arranged CdS/ZnS-TiO<sub>2</sub> photoanode and air-breathing CuO photocathode for simultaneous wastewater treatment and electricity generation, *Sep. Purif. Technol.* 229 (2019), 115821, <https://doi.org/10.1016/j.seppur.2019.115821>.
- [28] Z.A. Gu, J. Zhou, X.Q. An, Q. Chen, C.Z. Hu, H.J. Liu, J.H. Qu, A dual-biomimetic photocatalytic fuel cell for efficient electricity generation from degradation of refractory organic pollutants, *Appl. Catal. B Environ.* 298 (2021), 120501, <https://doi.org/10.1016/j.apcatb.2021.120501>.
- [29] N. Nordin, L.N. Ho, S.A. Ong, A.H. Ibrahim, S.L. Lee, Y.P. Ong, Elucidating the effects of different photoanode materials on electricity generation and dye degradation in a sustainable hybrid system of photocatalytic fuel cell and peroxi-coagulation process, *Chemosphere* 214 (2019) 614–622, <https://doi.org/10.1016/j.chemosphere.2018.09.144>.
- [30] X.F. He, X. Chen, R. Chen, X. Zhu, Q. Liao, D.D. Ye, Y.X. Yu, W. Zhang, J.W. Li, A 3D oriented CuS/Cu<sub>2</sub>O/Cu nanowire photocathode, *J. Mater. Chem. A* 9 (2021) 6971–6980, <https://doi.org/10.1039/d0ta11020e>.
- [31] Y.Z. Zhang, L.F. Liu, B. Van der Bruggen, M.K.H. Leung, F.L. Yang, A free-standing 3D nano-composite photo-electrode—Ag/ZnO nanorod arrays on Ni foam effectively degrade berberine, *Chem. Eng. J.* 373 (2019) 179–191, <https://doi.org/10.1016/j.cej.2019.05.026>.
- [32] B.Q. Deng, S.Z. Fu, Y.P. Zhang, Y. Wang, D.M. Ma, S.S. Dong, Simultaneous pollutant degradation and power generation in visible-light responsive photocatalytic fuel cell with an Ag-TiO<sub>2</sub> loaded photoanode, *Nano-Struct. Nano-Objects* 15 (2018) 167–172, <https://doi.org/10.1016/j.nano.2017.09.011>.
- [33] Y.Q. Su, Y.L. Wang, L.G. Xia, W.F. Yao, Q. Wu, Y.L. Min, Q.J. Xu, 3D coral-like Fe doped NiCo<sub>2</sub>S<sub>4</sub> cathode for stable high-efficiency photoelectrochemical tetracycline degradation and simultaneous energy recovery, *Chem. Eng. J.* 449 (2022), 137867, <https://doi.org/10.1016/j.cej.2022.137867>.
- [34] D.Z. Kong, Y. Wang, S.Z. Huang, B. Zhang, Y.V. Lim, G.J. Sim, P.V.Y. Alvarado, Q. Ge, H.Y. Yang, 3D printed compressible quasi-solid-state nickel-iron battery, *ACS Nano* 14 (2020) 9675–9686, <https://doi.org/10.1021/acsnano.0c01157>.
- [35] B. Yao, S. Chandrasekaran, H.Z. Zhang, A. Ma, J.Z. Kang, L. Zhang, X.H. Lu, F. Qian, C. Zhu, E.B. Duoss, C.M. Spadaccini, M.A. Worsley, Y. Li, 3D-printed structure boosts the kinetics and intrinsic capacitance of pseudocapacitive graphene aerogels, *Adv. Mater.* 32 (2020), 1906652, <https://doi.org/10.1002/adma.201906652>.
- [36] Z.P. Yang, S.M. Jia, Y.T. Niu, X.T. Lv, H.L. Fu, Y.Y. Zhang, D.P. Liu, B. Wang, Q. W. Li, Bean-pod-inspired 3D-printed phase change microlattices for solar-thermal energy harvesting and storage, *Small* 17 (2021), 2101093, <https://doi.org/10.1002/smll.202101093>.
- [37] D.X. Cao, Y.J. Xing, K. Tantratian, X. Wang, Y. Ma, A. Mukhopadhyay, Z. Cheng, Q. Zhang, Y.C. Jiao, L. Chen, H.L. Zhu, 3D printed high-performance lithium metal microbatteries enabled by nanocellulose, *Adv. Mater.* 31 (2019), 1807313, <https://doi.org/10.1002/adma.201807313>.
- [38] X.L. Li, S.W. Ling, W.Q. Cao, L. Zeng, R.X. Yuan, C.H. Zhang, Surface-adaptive capillarity enabling densified 3D printing for ultra-high areal and volumetric energy density supercapacitors, *Angew. Chem. Int. Ed.* 61 (2022), e202202663, <https://doi.org/10.1002/anie.202202663>.
- [39] B. Yao, H.R. Peng, H.Z. Zhang, J.Z. Kang, C. Zhu, G. Delgado, D. Byrne, S. Faulkner, M. Freyman, X.H. Lu, M.A. Worsley, J.Q. Lu, Y. Li, Printing porous carbon aerogels for low temperature supercapacitors, *Nano Lett.* 21 (2021) 3731–3737, <https://doi.org/10.1021/acs.nanolett.0c04780>.
- [40] B. Yao, S. Chandrasekaran, J. Zhang, W. Xiao, F. Qian, C. Zhu, E.B. Duoss, C. M. Spadaccini, M.A. Worsley, Y. Li, Efficient 3D printed pseudocapacitive electrodes with ultrahigh MnO<sub>2</sub> loading, *Joule* 3 (2019) 1–12, <https://doi.org/10.1016/j.joule.2018.09.020>.
- [41] W.B. Kang, L. Zeng, S.W. Ling, R.X. Yuan, C.H. Zhang, Self-healable inks permitting 3D printing of diverse systems towards advanced bicontinuous supercapacitors, *Energy Storage Mater.* 35 (2021) 345–352, <https://doi.org/10.1016/j.ensm.2020.11.032>.
- [42] C.L. Chen, J.M. Jiang, W.J. He, W. Lei, Q.L. Hao, X.G. Zhang, 3D printed high-loading lithium-sulfur battery toward wearable energy storage, *Adv. Funct. Mater.* 30 (2020), 1909469, <https://doi.org/10.1002/adfm.201909469>.
- [43] Y.Q. Jiang, Z. Xu, T.Q. Huang, Y.J. Liu, F. Guo, J.B. Xi, W.W. Gao, C. Gao, Direct 3D printing of ultralight graphene oxide aerogel microlattices, *Adv. Funct. Mater.* 28 (2018), 1707024, <https://doi.org/10.1002/adfm.201707024>.
- [44] M.W. Peng, Z. Wen, L.J. Xie, J. Cheng, Z. Jia, D.L. Shi, H.J. Zeng, B. Zhao, Z. Q. Liang, T. Li, L. Jiang, 3D printing of ultralight biomimetic hierarchical graphene materials with exceptional stiffness and resilience, *Adv. Mater.* 31 (2019), 1902930, <https://doi.org/10.1002/adma.201902930>.
- [45] Z.P. Yang, X.T. Lv, C.J. Zhang, Y.Y. Zhang, S.M. Jia, Y.T. Niu, Y.C. Zhang, B. Wang, T. Zhao, H.L. Fu, Q.W. Li, Core-sheath 3D printing of highly conductive and MoS<sub>2</sub>-loaded electrode with pseudocapacitive behavior, *Chem. Eng. J.* 423 (2021), 130304, <https://doi.org/10.1016/j.cej.2021.130304>.
- [46] X.W. Tang, H. Zhou, Z.C. Cai, D.D. Cheng, P.S. He, P.W. Xie, D. Zhang, T.X. Fan, Generalized 3D printing of graphene-based mixed-dimensional hybrid aerogels, *ACS Nano* 12 (2018) 3502–3511, <https://doi.org/10.1021/acsnano.8b00304>.
- [47] R.B. Zhu, Y.Z. Zhu, F.D. Chen, R. Patterson, Y.Z. Zhou, T. Wan, L. Hu, T. Wu, R. Joshi, M.Y. Li, C. Cazorla, Y.R. Lu, Z.J. Han, D.W. Chu, Boosting moisture induced electricity generation from graphene oxide through engineering oxygen-based functional groups, *Nano Energy* 94 (2022), 106942, <https://doi.org/10.1016/j.nanoen.2022.106942>.
- [48] Y. Wang, Y. Zhang, Z. Zhang, T. Li, J. Jiang, X.H. Zhang, T.X. Liu, J.L. Qiao, J. Huang, W.F. Dong, Pistachio-inspired bulk graphene oxide-based materials with shapeability and recyclability, *ACS Nano* 16 (2022) 3394–3403, <https://doi.org/10.1021/acsnano.2c00281>.